Investigation on the Mechanical Properties and Shape Memory Effect of Landing Buffer Structure Based on NiTi Alloy Printing

Zhenglei Yu

  Jilin University State Key Laboratory of Automotive Simulation and Control

Renlong Xin

  jilin university,kay lab of bionic engineering,ministry of education

Zezhou Xu

  key lab of bionic engineering,ministry of education,jilin university

Yining Zhu

  agriculture college,yanbian university

Xiaolong Zhang

  key lab of bionic engineering,ministry of education

Shijie Hao

  China University of Petroleum Beijing State Key Laboratory of Heavy Oil Processing

zhihui zhang (✉ zhzh@jlu.edu.cn)

  key lab of bionic engineering,ministry of education,jilin university

Ping Liang

  key lab of bionic engineering,ministry of education

Original Article

Abstract

With the deepening of human research on deep space exploration, our research on the soft landing methods of landers has gradually deepened. Adding a buffer and energy-absorbing structure to the leg structure of the lander has become an effective design solution. Based on the energy-absorbing structure of the leg of the interstellar lander, this paper studies the appearance characteristics of the foot-grabbing of the Odontodactylus scyllarus. The foot-grabbing of the Odontodactylus scyllarus can not only hit the prey highly when preying, but also can easily withstand the huge counter-impact force. the predatory foot structure of the Odontodactylus scyllarus, like a symmetrical cone, shows excellent rigidity and energy absorption capacity. Inspired by this discovery, we used SLM technology to design and manufacture two nickel-titanium samples, which respectively showed high elasticity, shape memory, and better energy absorption capacity. This research provides an effective way to design and manufacture high-mechanical energy-absorbing buffer structures using bionic 3D printing technology and nickel-titanium alloys.

Highlights

1. The new landing buffer structure based on bionics has outstanding effect of energy absorption and shock absorption
2. The application of SLM technology allows us to print NiTi alloy structures with excellent properties.
3. NiTi alloys are used as structural materials to enhance the mechanical properties of the structures. Meanwhile, the structure is endowed with unique self-recovery performance

1. Introduction

Soft landing on the surface of asteroids is a key challenge in the field of deep space exploration. In the case of a lunar landing, the spacecraft needs to land without aerodynamic deceleration on the surface of the moon. Thus, it must rely on its own propulsion system to gradually reduce its speed so that it can land safely in a predetermined area. The landing speed cannot be reduced to zero when the lander has a full contact with the lunar surface, and the lander is subjected to heavy impact loads upon landing. So, it is necessary to add an auxiliary landing buffer system to absorb the remaining kinetic energy over a limited distance. Zeng et al. [1] modified the dynamics analysis model by using the groun experiment results from a simulated lander and found that the structure of the lander and the flexibility of the buffer mechanism have a great impact on the buffer performance. Yan et al. [2] analyzed the factors that influence the landing buffer characteristics in the soft-landing process of a reusable vehicle for vertical take-off and landing. The simulation analysis of a honeycomb buffer was carried out, and the deformation and buffering characteristics in the process of honeycomb crushing were discussed. Van et al. [3] developed and proposed a fast, parallel simulation of the lander/rover bounce deployment on asteroids or comets. The collision and contact motion between a probe with arbitrary shape/inertia and a target body was studied. At present, scholars domestic and abroad have done a lot of research on landing modes for controlling landers and impact buffers during landing, and the research on the

supporting legs of landers is mainly focused on the research [4–8] and development of the mechanical structures [9–11]. However, there is an urgent need for research on the structure design of the supporting legs and its reusability.

In the lengthy process of biological evolution, a variety of organisms gradually developed unique structures to adapt to the environment. These structures and their functions tend to be perfect, providing a reference for solving many modern engineering problems. For example, the sea world's "boxer" the Odontodactylus scyllarus has two highly developed the Predatory Foot (PF) which can not only crush the defense of prey at a speed of 80 kilometers per hour, but also disperse and transfer energy while generating impact load due to its unique structure to achieve the effect of energy absorption, so that shrimp can withstand the impact of more than 700 N [12–14]. Therefore, the research on the mechanism of load absorption in the forefoot structure of mantis shrimp will have an important impact on the development of the field of shock absorption and cushioning structure. Patek et al. [15] studied the energy release process of mantis shrimp during a single punch and the elastic mechanism of mantis shrimp which is composed of exoskeleton and controlled by latch mechanism. James [16] studied the morphological characteristics of foot predation of mantis shrimp. Guo et al. [17] designed a corresponding bionic sandwich structure for armor protection. As shown in Fig. 1, the obvious sandwich structure of the mantis shrimp feet makes it incredibly impact resistant,which provide a good model for us to design impact resistant structures.

Due to its excellent shape memory effect and superelasticity, NiTi has attracted wide attention of scholars at home and abroad. It's their poor machinability limit its application in structural parts. In this regard, many scholars use Additive Manufacturing (AM) to manufacture NiTi alloy structures and parts [18–22]. Through AM technology, structural parts can be printed directly, avoiding the post-processing process, and components can be directly formed. SLM-NiTi is widely used in porous structures owing to its excellent biocompatibility and elastic modulus close to the human body [23–25]. However, the research on bionic structures with shape memory effect and hyperelasticity is relatively scarce. Ma et al. [26] reported the bionic structure of NiTi crab claws by using SLM, and separately studied the effects of different pore distribution forms on energy absorption. It was found that three different pore distribution modes significantly improved the toughness of Nitinol part and showed similar energy absorption capabilities. The recovery rate of NiTi structure parts found by Xiong et al. [27] can reach 99% under 50% large deformation. SLM-NiTi has a profound research value in bionic structure and shape memory effect.

This paper aims to study a SLM-NiTi bionic energy-absorbing structure, which can be restored and recycled after heating. Taking Odontodactylus scyllarus foot prey sandwich structure as the bionic research object, the model was established using CATIA, a 3D modeling software, and the simulation analysis was carried out by finite element analysis software under the load condition. Then the structure prototype was prepared by the 3D printing technology, and the mechanical properties of the prototype were experimented. By comparing the simulation data, the stress-strain relationship of the structural model under axial compression and unloading under different working conditions was analyzed, and the

bearing capacity and recovery performance of the model were studied. The accuracy of the simulation analysis and the effectiveness of the method were verified by comparing with the experimental results. Then the Cell Structure (CS) was upgraded to the and the Double Layer Structure (DLS), and the finite element model and solid model of the DLS were established. By numerical simulation and experimental experiment, the absorbing capacity of the DLS under the same loading and unloading conditions was obtained.

2. Materials And Methods

2.1 Material Selection

$Ni_{50.8}Ti_{49.2}$ alloy powders ($Ni_{50.8}Ti_{49.2}$ powders with particle size between 13 μm and 53 μm prepared by electrode induction-molten gas atomization (EIGA) process) were selected for printing. In the printing process, high purity argon gas is used as the protective gas to reduce the oxygen content in the manufacturing chamber.

Fig. 2 is the characteristic analysis of the alloy powder we selected. It can be seen from Fig. 2a that the alloy powder we used has a high sphericity, which is conducive to the melting of the metal powder bed. Fig. 2b shows the particle size distribution of $Ni_{50.8}Ti_{49.2}$ alloy powder, from which we can see that the particle size of the powder is less than 22.2μm accounts for 10%, and the particle size is greater than 58.1μm accounts for 10%. The particle size distribution of this batch of powder has a wide main peak near the average particle size d_{50}=36.8μm, which indicates that the powder has a good uniformity. Fig. 2c shows the DSC curve of $Ni_{50.8}Ti_{49.2}$ powder. The initial temperature (M_S) and termination temperature (M_f) of martensitic phase transformation are 24.8°C and -16.7°C, respectively. The initial temperature (A_S) and termination temperature (A_f) of austenitic phase transformation are -25.3°C and 54.9°C, respectively.

2.2. The architecture of the energy-absorbing structures

It was observed under the Stereo Microscope that the PF of Odontodactylus scyllarus had a cone-shaped structure. According to the bionic design principle, took Odontodactylus scyllarus as the biological model, the landing buffer bionic model was established by using CATIA software. The outer width (*L*), overall height (*H*), support thickness (*T*) and support width (*W*) of the CS were 26mm, 18mm, 0.5mm, and 3mm, respectively. The width (*L*), overall height (*H*), support thickness (*T*) and support width (*W*) of the DLS model are 23mm, 17mm, 0.6mm and 1.5mm, respectively (see Table. 1)

As shown in Table. 2, in order to reduce the cost and time of real-time experiments, and conduct further research, the nonlinear explicit finite element (FE) code LS-DYNA is employed to simulate the uniform quasi-static compression. In the finite element model, the S/R quadratic tetrahedron element with Nodal Rotations is used, while the Fully integrated shell element is used in the shell element. Among them, the element size of the CS is 0.3mm, and the element size of the DLS is 0.1mm.

After the node set constraint is carried out at the bottom of the model, the rigid wall simulates the load-unload process of the model with reference to the load curve, so that the numerical simulation can describe its dynamic process relatively accurately. The relevant parameters of each module material are shown in Table. 2.

2.3 Additive manufacturing of landing buffer bionic model prototype

The SLM-NiTi (Ni: 55.8wt%) sample was fabricated from the gas-atomized powder with particles of 15-53μm in diameter and built on the NiTi substrate maintained at 180°C. SLM processing was carried out in argon gas with overpressure of 10~12 mbar and oxygen level below 500 ppm. The adopted Eplus M100-T machine is equipped with a maximum 200 W laser of 50μm in diameter. The parameters used for preparing samples were: laser power of 120W, laser scanning speed of 600mm s^{-1}, layer thickness of 30μm, hatch spacing of 80μm. In the aspect of powder material selection, NiTi powder with corresponding ratio was prepared by coating method. The samples prepared by strip zoning strategy and optimized process parameters showed excellent chemical stability, high elastic modulus, high corrosion resistance and shape memory. NiTi alloy (Ni:55.8wt%) was used as the matrix material. The sample prepared is shown in Fig. 2a and Fig. 2b Due to the excellent mechanical properties of NiTi shape memory alloy, the resulting structure not only has the characteristics of compression, buffering and energy absorption, but also has good recoverability after compression.

2.4 Experimental details

The Force-Displacement curve was recorded during the quasi-static compressive loading experiment. The prototype was placed in the central position of the experiment bed, and the actual sample experiment process was standardly performed. The Force-Time curve between the static pressure load and the sample was measured by the force sensor. Pressing down the sample at a rate of 4mm per minute. The temperature in the laboratory is 20 °C. As shown in Fig. 3, the rigid loading plate was pressed on the sample according to the direction of gravity to ensure uniform distribution of impact force.

Phase transformation temperature was investigated by using TA Instruments Q20 DSC instrument at a heating/cooling rate of 5 °C/min^{-1} from -70 °C to 100 °C. X-ray diffractometer (XRD, Shimadzu, 6100) was used in analyzing the phase structure. And being compressed at room temperature, heating above the A_f point in water at 100 °C to verify its shape memory effect.

3. Results And Discussions
3.1 Phase structure

As shown in Fig. 3a, the DSC graph shows the Ms is 29.28 °C, M_f is -9.66 °C upon cooling, and the A_s is 27.81 °C, A_f is 63.41 °C upon heating. And Fig. 3b shows the XRD pattern of the SLM-NiTi, which demonstrates the sample remains B2 austenite state and B19' martensite state at room temperature

(20°C), mainly B2 austenite state. The results consistent with the DSC curve, which proves that the printed material is in B2 austenite state at room temperature with a small amount of B19' martensite phase.

The tensile stress-strain curve of SLM-NiTi is shown in Fig. 3C. The tensile yield strain of the sample is 1.13%, and the yield strength is 193.1 MPa. The fracture strain is 10.89% and the fracture strength is 735.18 MPa. It can be seen from the figure that a typical stress platform appears after the yield point due to the martensite orientation deformation during the tensile process. The tensile process of the sample is divided into four stages, which are the initial elastic deformation (stage I), the stress platform caused by martensite orientation deformation (stage II), the elastic deformation of directional martensite (stage III), and the elastic-plastic deformation of directional martensite (stage IV).

3.2 Deformation behaviour

Another key measurable output from the finite element simulation and experimental work is the deformation mode of the two structures. Figure 4 shows the deformation process of the quasi-static compressive loading of the CS and DLS. In the early stage of pressure under the rigid loading plate, the unit structure hardly showed obvious deformation due to the strength of NiTi shape memory alloy. Because the CS is placed in the middle of the experiment bed, it is equivalent to restricting the z-direction displacement of the bottom of the bracket only. The energy is absorbed by the structure in a controllable way through regular deformation patterns of the two structures. The deformation modes observed in the experiment are compared with those calculated by finite element simulation.

3.3 Study on mechanical properties and shape memory recovery characteristics

As shown in Fig. 5, equivalent von Mises stress and deformed configurations obtained from FE analysis for two structures. Figure 6a and Fig. 6c respectively shows the FDT curves obtained from the loading-unloading-heating process of the two structures in the simulation analysis and experiment. The two curves can be divided into three parts: loading, unloading and deformation recovery. Firstly, in the loading and unloading part of the curve, the numerical simulation and the experimental data curve have a high consistency. As can be seen in the force displacement curve is given, the compression process can be divided into two stages, the first stage, the bearing capacity of the two structures increased with the increase of the compression displacement of relationship, a kind of approximate linear increase in overall is a kind of elastic stage, Stress concentration occurs at the upper part of the CS and the middle joint of the DLS (Fig. 5). When the load reaches the value of P_{max} (point B and point B_1 of Fig. 6), it enters the second stage, and local buckling instability occurs from the upper connection of the CS, resulting in plastic deformation. With the increase of compression displacement, the buckling of the structure gradually diffused to the whole leg. However, before the loading displacement was about 1.1mm (point B_1), the deformation of the DLS was mainly dominated by the elastic deformation of the lower layer bracket. The deformation of the structure increased with the increase of the compression displacement,

and the load presented a linear increasing trend. Later, due to excessive structural deformation, the lower support appears buckling deformation, and the supporting force of the lower support is dominated by the bending moment of the support (Fig. 5). As the bending Angle of the support increases, the supporting force provided by the support becomes smaller, so the load curve shows a downward trend.

In Fig. 6b, with the reduction of load, the shape of the CS gradually recovered, and elastic recovery rate reached about 84%, This is mainly due to the presence of the B2 austenite phase at room temperature, which gives the material part of the superelasticity, so that it has a certain shape recovery after unloading. It is found that the consistency of the simulation results with the experimental results is close to 90%. The results show that the simulation analysis technique can better simulate the deformation process of the NiTi memory alloy double-layer composite module in the process of static crushing, unloading and spring back, to better predict its bearing capacity. After unloading, the elastic recovery rate of the sample reaches 84%, the sample was put into a beaker with hot water (~ 100°C), the SLM-NiTi sample exhibits shape recovery rate of 99%. The reason for the shape recovery after heating is that part of the B19' martensite has undergone heat-induced martensite transformation. It can be inferred that although the total deformation is 70%, the deformation in some areas is much lower than 70%, and it may have only undergone martensitic transformation redirection without plastic deformation. Therefore, the deformed part can be restored to its original shape after heating.

In Fig. 5 and Fig. 6d, the compression process and experimental results of the DLS were further analyzed. In the process of pressing the rigid plate, the deformation first appears in the lower bracket, the edge of the lower bracket opens to the surrounding, while the upper bracket does not show obvious deformation, indicating that the strength of the upper bracket is obviously greater than that of the lower bracket. When pressed down for 3mm, the lap positions of the upper and lower brackets become brittle, resulting in structural instability and the end of the experiment. In this scheme, the support has a thickness of 0.6mm, a width of 1.5mm and a thickness to width ratio of 2:5. In the future, the thickness to width ratio will be reduced, and the support will be designed to be a structure similar to a thin plate as possible to give full play to its hyperelasticity characteristics and avoid premature brittle fracture of the 3D printed structure. Also, compression loading should be withdrawn after the downforce displacement reaches 3mm. In a word, the deformation order of the structure is basically bottom-up. Therefore, in order to improve the bearing capacity of the whole structure or control the deformation sequence of the structure, a support with the lower strength should be chosen. In this study, the quasi-static compressive loading simulation analysis was carried out on the two-layer module, and the whole deformation process of the module was simulated during the loading stage, providing a basis for optimizing nickel titanium alloy in multivariable and multiparameter modules in the future.

There is a slight difference between the simulation analysis and the experiment during loading. Before the loading displacement was about 1.1mm (point B), the deformation of the double-layer structure was mainly dominated by the elastic deformation of the lower layer bracket. The deformation of the structure increased with the increase of the compression displacement, and the load presented a linear increasing trend. Later, due to excessive structural deformation, the lower support appears buckling deformation,

and the supporting force of the lower support is dominated by the bending moment of the support. As the bending Angle of the support increases, the supporting force provided by the support becomes smaller, so the load curve shows a downward trend. The final state after unloading is similar to the CS. As shown in Fig. 6a and Fig. 6c, When the structure produces shape memory recovery under the action of thermal excitation, the structure under the deformation state exhibits different recovery efficiency at different temperatures. In experiment, we observed that the DLS rapidly recovered its shape within a few seconds after being stimulated by heat and achieved a recovery rate of about 98%. Therefore, it can be concluded that the DLS has excellent reusable performance.

3.4. Performance indicators

Different parameters are used to compare the performance of various devices. The indicators used within this study include Peak Force (P_{max}); Energy Absorption (EA); Specific Energy Absorption (SEA); and shape recovery rate.

The peak force is the force required to initiate plastic deformation within the tube and hence begin the energy absorption. Total energy absorption through plastic deformation is calculated as the area under the force-displacement curve, using Eq. (1):

$$EA = \int_0^d P(x)dx \qquad (1)$$

where d is the total structural volume, P is static force, x is the instantaneous crush displacement.

Given that mass is a key indicator in any automotive structural design, specific energy absorption provides an indicator of the EA per unit mass, as presented in Eq. (2). A high EA and SEA are highly desirable within crashworthy applications.

$$SEA = \frac{EA}{M} \qquad (2)$$

where M is the structural mass.

3.5. Post-compression analysis

The experimental percentage crush and corresponding reaction force were generated from the experiment machine. The recorded Performance indicator are listed in Table 3, including the P_{max}, EA, SEA, M, Compressible rate and shape recovery rate.

From Table. 3, it may be observed that DLS has excellent mechanical properties, but its compressible deformation is small. On the contrary, although CS has weak mechanical properties, its compressible deformation can reach 66.67%, and its shape recovery rate can reach 99% after thermal excitation.

4. Conclusions

In this paper, a recoverable nickel-titanium alloy landing buffer bionic structure system was developed with the inspiration of the excellent impact energy absorption of Odontodactylus scyllarus's foot grazing.

presents a comprehensive investigation of the crashworthiness of simple hierarchical and fractal hierarchical structures using experimental experiments and computational modeling techniques. Several conclusions are drawn from the results:

(1) It is of great theoretical and practical significance to improve the structure of lander shock absorber by printing biomimetic model based on additive manufacturing technology. The structure is based on Nitinol and has good shape memory recovery performance, which provides an effective solution for the efficient reuse of the lander. This is the key to achieving continuous protection after any initial interference.

(2) The experiment and simulation of the unit structure show that the CS has very high elasticity although it is not outstanding in carrying capacity, which provides a good idea for the study of buffer structure. when the bionic DLS is pressed down by about 38.9 %, the peak load of the DLS is 692 N. Compared with the CS, in the loading and unloading process, the DLS shows a higher capacity of load and absorption.

(3) This study helps us to understand the deformation pattern and interlayer strength distribution of each structure, provides an important basis for the optimal design of each layer and the deformation control of the entire module, and lays a foundation for the extended application and performance design of multi-layer NiTi alloys.

Declarations

Availability of data and materials

The data and materials that support the findings of this study are available from the corresponding author upon reasonable request.

Competing interests

We declare that we have no financial and personal relationships with other people or organizations that can inappropriately influence our work, there is no professional or other personal interest of any nature or kind in any product, service and/or company that could be construed as influencing the position presented in, or the review of the manuscript entitled.

Funding

Not applicable

Authors' contributions

Zhenglei Yu⬜ Conceptualization, Methodology, Writing - Original Draft, Validation. Renlong Xin⬜ Data curation, Writing-Original draft preparation, Software, Zezhou Xu⬜ Investigation, Term. Yining Zhu⬜ Investigation. Xiaolong Zhang⬜ Visualization. Shijie Hao⬜ Supervision, Resources. Zhihui Zhang⬜ Validation, Project administration, Resources. Ping Liang⬜ Supervision.

Acknowledgements

References

1. Zeng FM, Yang JZ, Zhu W, Chen TZ, Man JF, Xu QH. Research on design method of lunar Lander landing buffer mechanism. Int J Spacecraft engineering 2010; 20: 46–51.

2. Yan Z. Design and analysis of outrigger buffers for vtol reusable launch vehicles. Harbin Institute of Technology 2019.

3. Van wal S, Reid RG, Scheeres DJ. Simulation of Nonspherical Asteroid Landers: Contact Modeling and Shape Effects on Bouncing. Int. J. Journal of Spacecraft and Rockets 2020; 57: 109–130.

4. Chen ZY, Imholz M, Li L, et al. Transient landing dynamics analysis for a lunar lander with random and interval fields. Applied Mathematical Modelling 2020; 88: 827–851.

5. Li RF, Guo WZ. Novel design of a family of legged mobile landers based on decoupled landing and walking functions. Journal of Mechanical Science and Technology 2020; 34: 3851–3822.

6. Huang MY. Control strategy of launch vehicle and lander with adaptive landing gear for sloped landing. Acta Astronautica 2019; 161: 509–523.

7. Ababneh MT, Tarau C, Anderson WG, Farmer JT. Thermal Control of Lunar and Mars Rovers/Landers Using Hybrid Heat Pipes. Journal of Thermophysics and Heat Transfer 2019; 33: 705–713.

8. Cheng B, Yu Y, Baoyin HX. Numerical simulations of the controlled motion of a hopping asteroid lander on the regolith surface. Monthly Notices of the Royal Astronomical Society 2019; 485: 3088–3096.

9. Huang MY. Control strategy of launch vehicle and lander with adaptive landing gear for sloped landing. Int. J. Acta Astronautica 2019; 161: 509–523.

10. Maeda T, Otsuki M, Hashimoto T. Protection against overturning of a lunar-planetary lander using a controlled landing gear. Int. J. Aerospace Engineering 2019; 233: 438–456.

11. Witte L, Roll R, Biele J, et al. Rosetta lander Philae - Landing performance and touchdown safety assessment. Acta Astronautica 2016; 125: 149–160.

12. Claverie T, Chan E, Patek SN. Modularity and scaling in fast movements: Power amplification in mantis shrimp. Evol Int J Org Evol 2011; 65: 443–461.

13. Patek SN, Caldwell RL. Extreme impact and cavitation forces of a biological hammer: Strike forces of the peacock mantis shrimp mantis shrimp. Int J Exp Biol 2005; 208: 3655–3664.

14. Knight K. Mantis shrimp pull punches in air for self-preservation. Journal of Experimental Biology 2020; 223.

15. Patek SN. The Power of Mantis Shrimp Strikes: Interdisciplinary Impacts of an Extreme Cascade of Energy Release. Integrative and Comparative Biology 2019; 59: 1573–1585.

16. Weaver JC, Milliron GW, Miserez A, Evans-Lutterodt K, Herrera S, Gallana I, et al. The Stomatopod Dactyl Club: A Formidable Damage-Tolerant Biological Hammer. Int J Science 2012; 336: 1275–1280.

17. Guo X, Dong XJ, Yu ZL, Zhang ZH, Xie XY, Wang XB,et al. Study on the Mechanical Properties of Bionic Protection and Self-Recovery Structures. Int J Materials 2020; 13.

18. Xiong F, Yang HF, Liu K, Man JX, Chen HX. Forming and two-way shape memory effect of NiTi alloy induced by laser shock imprinting. Optics and Laser Technology 2019; 120.

19. Bimber BA, Hamilton RF, Keist J, Palmer TA. Anisotropic microstructure and superelasticity of additive manufactured NiTi alloy bulk builds using laser directed energy deposition. Materials Science and Engineering a-Structural Materials Properties Microstructure and Processing 2016; 674: 125–134.

20. Elahinia M, Moghaddam NS, Andani MT, Amerinatanzi A, Bimber BA, Hamilton RF. Fabrication of NiTi through additive manufacturing: A review. Progress In Materials Science 2016; 83: 630–663.

21. Biffi CA, Bassani P, Fiocchi J, Tuissi A. Microstructural and Mechanical Response of NiTi Lattice 3D Structure Produced by Selective Laser Melting. Metals 2020; 10.

22. Van Humbeeck J. Additive Manufacturing of Shape Memory Alloys. Shape Memory and Superelasticity 2018; 04 309–312.

23. Andani MT, Saedi S, Turabi AS, Karamooz MR, et al. Mechanical and shape memory properties of porous Ni50.1Ti49.9 alloys manufactured by selective laser melting. J Mech Behav Biomed Mater 2017; 68: 224–231.

24. Speirs M, Van Hooreweder B, Van Humbeeck J, Kruth JP. Fatigue behaviour of NiTi shape memory alloy scaffolds produced by SLM, a unit cell design comparison. J Mech Behav Biomed Mater 2017; 70: 53–59.

25. Dadbakhsh S, Speirs M, Kruth JP, Van Humbeeck J. Influence of SLM on shape memory and compression behaviour of NiTi scaffolds. CIRP Ann-Manuf Technol 2015; 64: 209–212.

26. Ma CL, Gu DD, Lin KJ, Dai DH, et al. Selective laser melting additive manufacturing of cancer pagurus's claw inspired bionic structures with high strength and toughness. Appl Surf Sci 2019; 469: 647–656.

27. Xiong ZW, Li ZH, Sun Z, Hao SJ, Yang Y, et al. Selective laser melting of NiTi alloy with superior tensile property and shape memory effect. J Mater Sci. Technol 2019; 35: 2238–2242.

Tables

Due to technical limitations, table 1 is only available as a download in the Supplemental Files section.

Table. 2 The related parameters of each module material.

Parameter	Rigid wall	Solid element	Shell element
P(t mm^{-3})	7.83×10^-9	6.45×10^-9	1×10^-11
E(Gpa)	207	18.555	210
μ	0.28	0.33	0.3
SIG_ASS(Mpa)		188.64	
SIG_ASF(Mpa)		353.02	
SIG_SAS(Mpa)		126.61	
SIG_SAF(Mpa)		57	
EPSL		0.07	

Table. 3 Comparison of Crashworthiness indicators for quasi-static compressive loading

Crashworthiness indicators	CS	DLS
M (g)	0.969	2.372
EA (J)	0.268	27.71
SEA (J g^{-1})	0.277	11.682
P_{max} (N)	7.2	634
shape recovery rate (%)	99	98
Compressible strain (%)	66.67	17.65

Figures
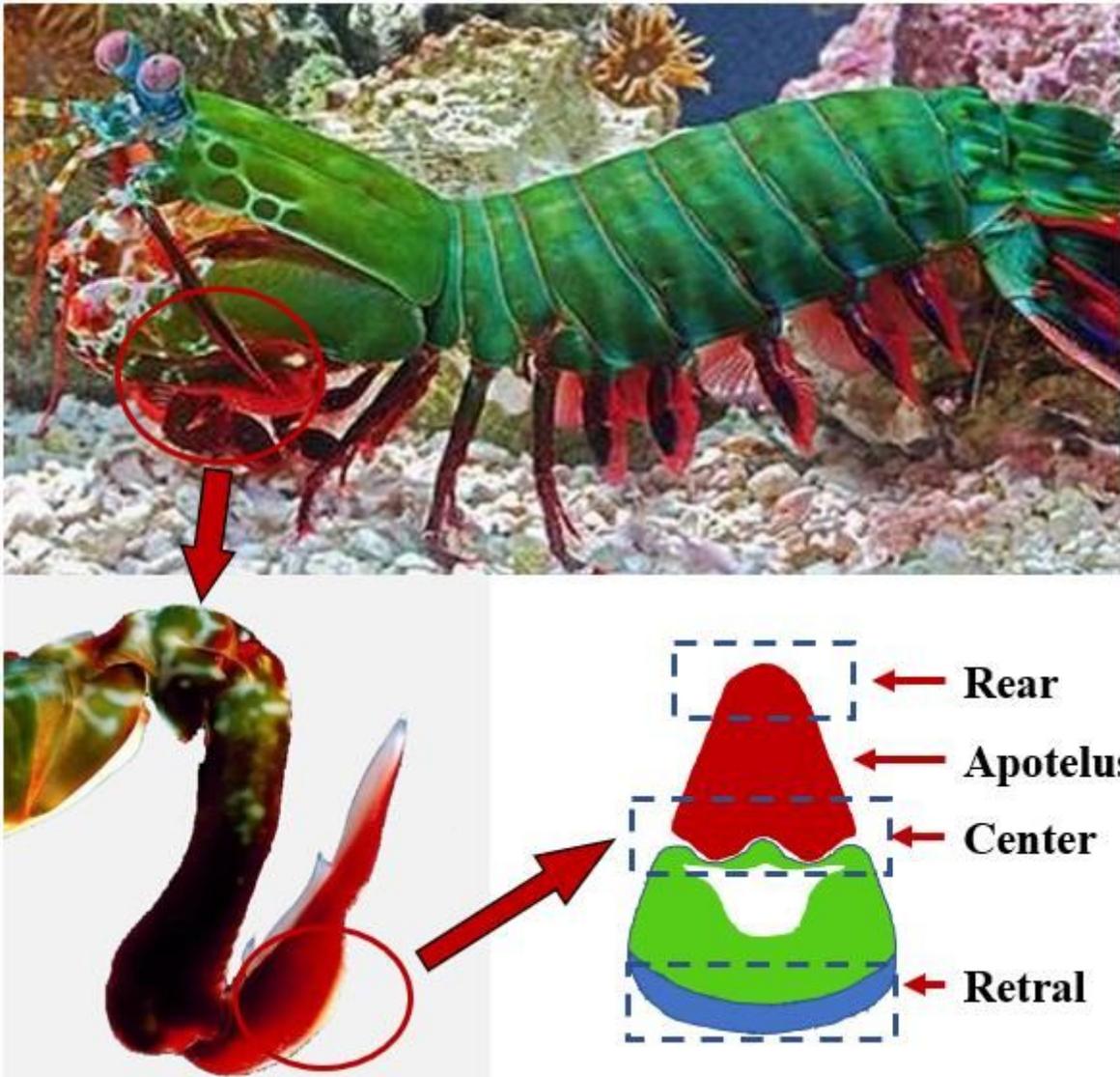
Figure 1

Structural diagram of the PF

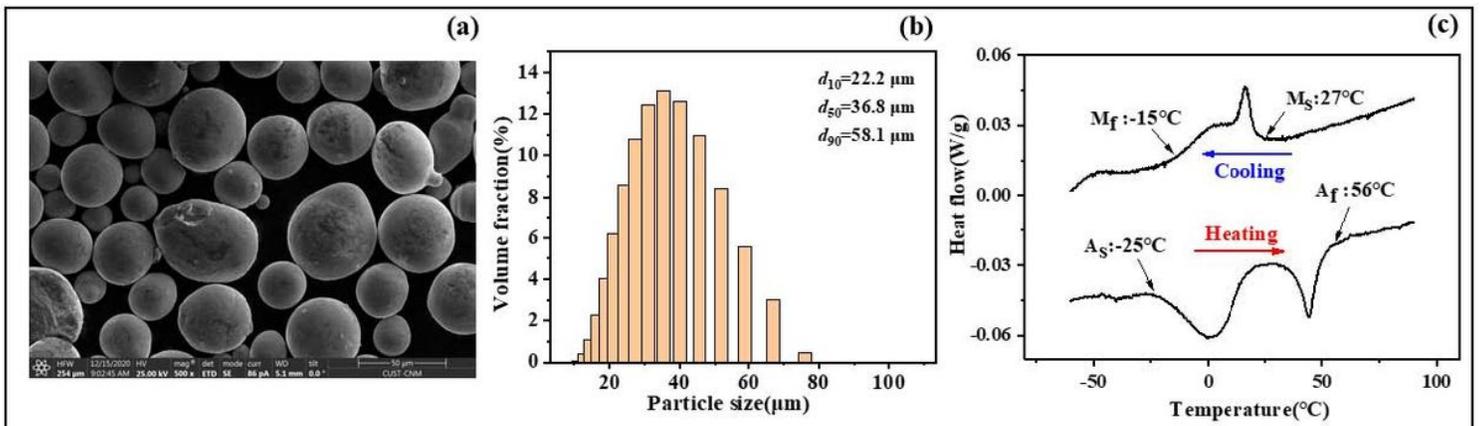**Figure 2**

Scanning electron microscope image (a), particle size distribution (b) and differential scanning calorimetry curves, c for Ni50.8Ti49.2 powder.
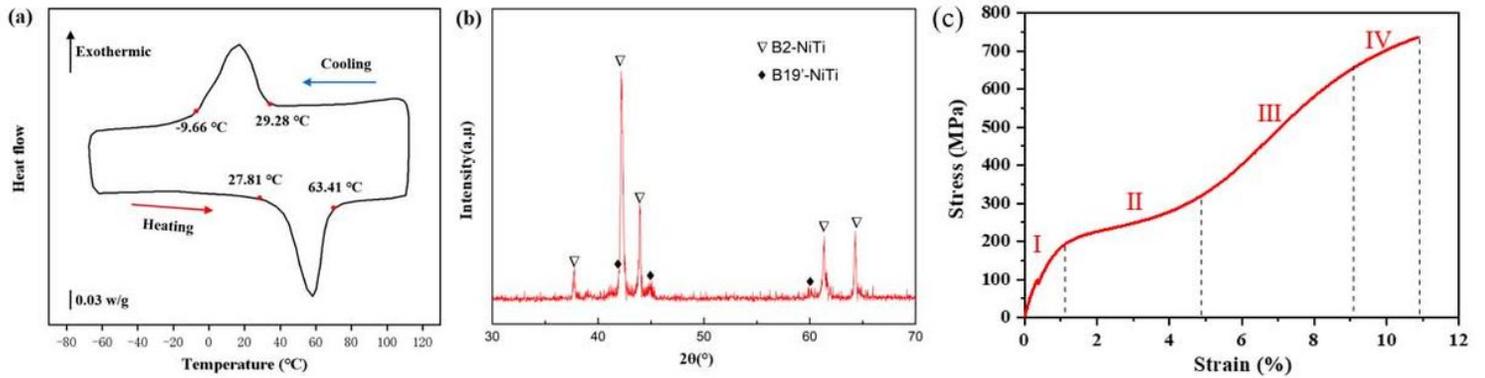

Figure 3

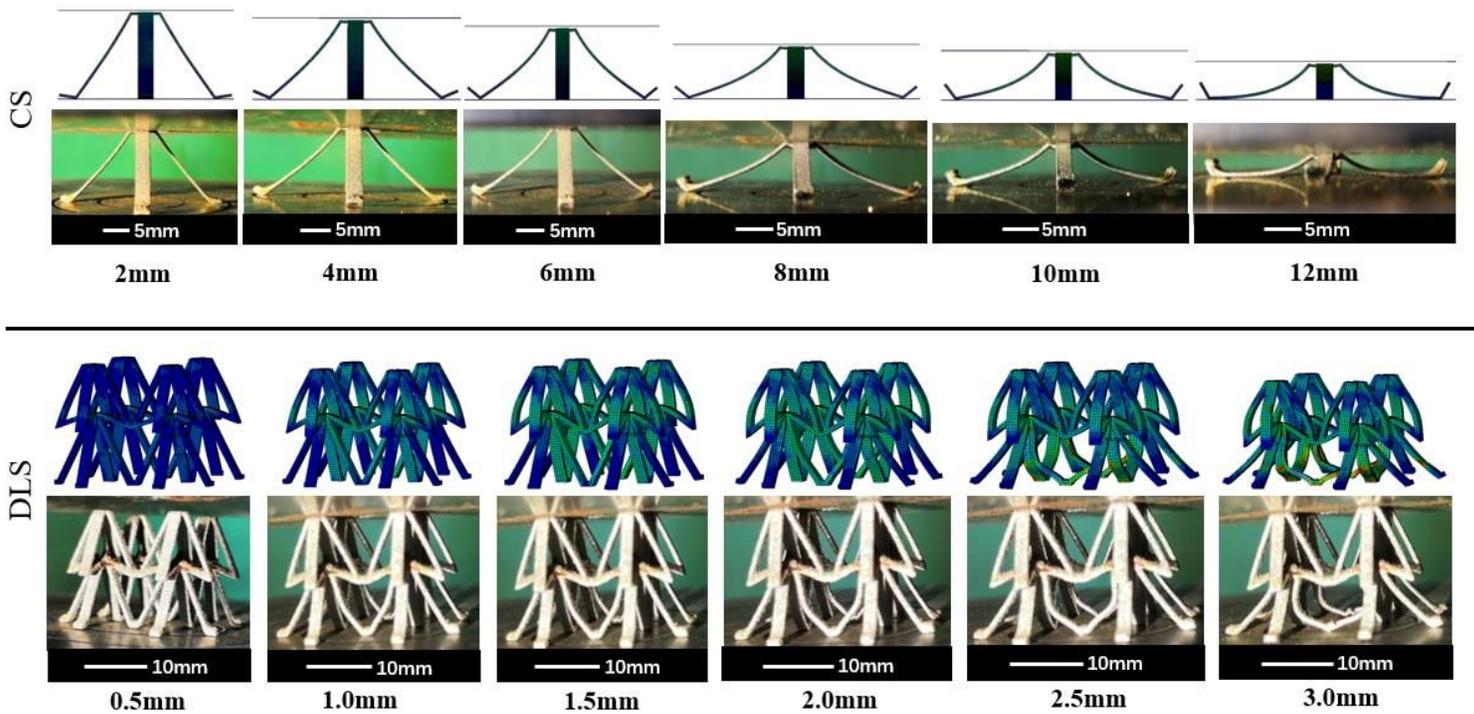(a) DSC graph of the SLM-NiTi and (b) XRD pattern of the SLM-NiTi. (c) Tensile stress-strain curve at RT

Figure 4

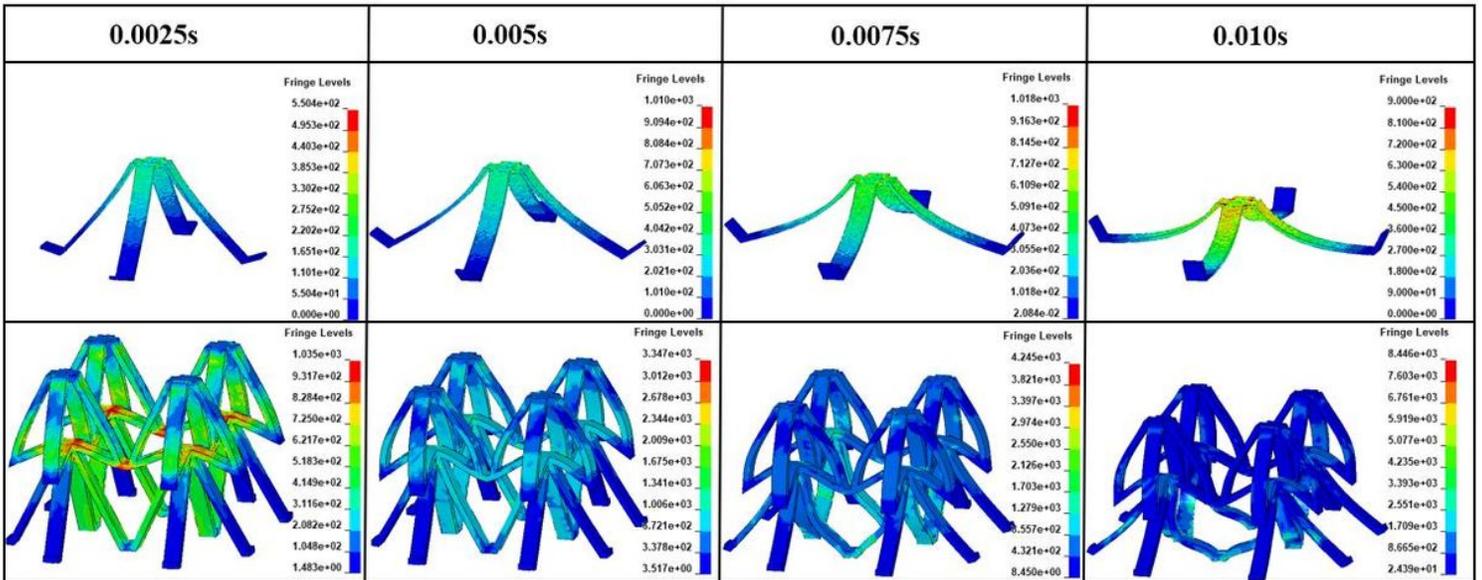Comparisons of the deformation of the bionic structures (CS and DLS) with the computational model.

Figure 5

Equivalent von Mises stress and deformed configurations obtained from FE analysis for the bionic structures (CS and DLS).
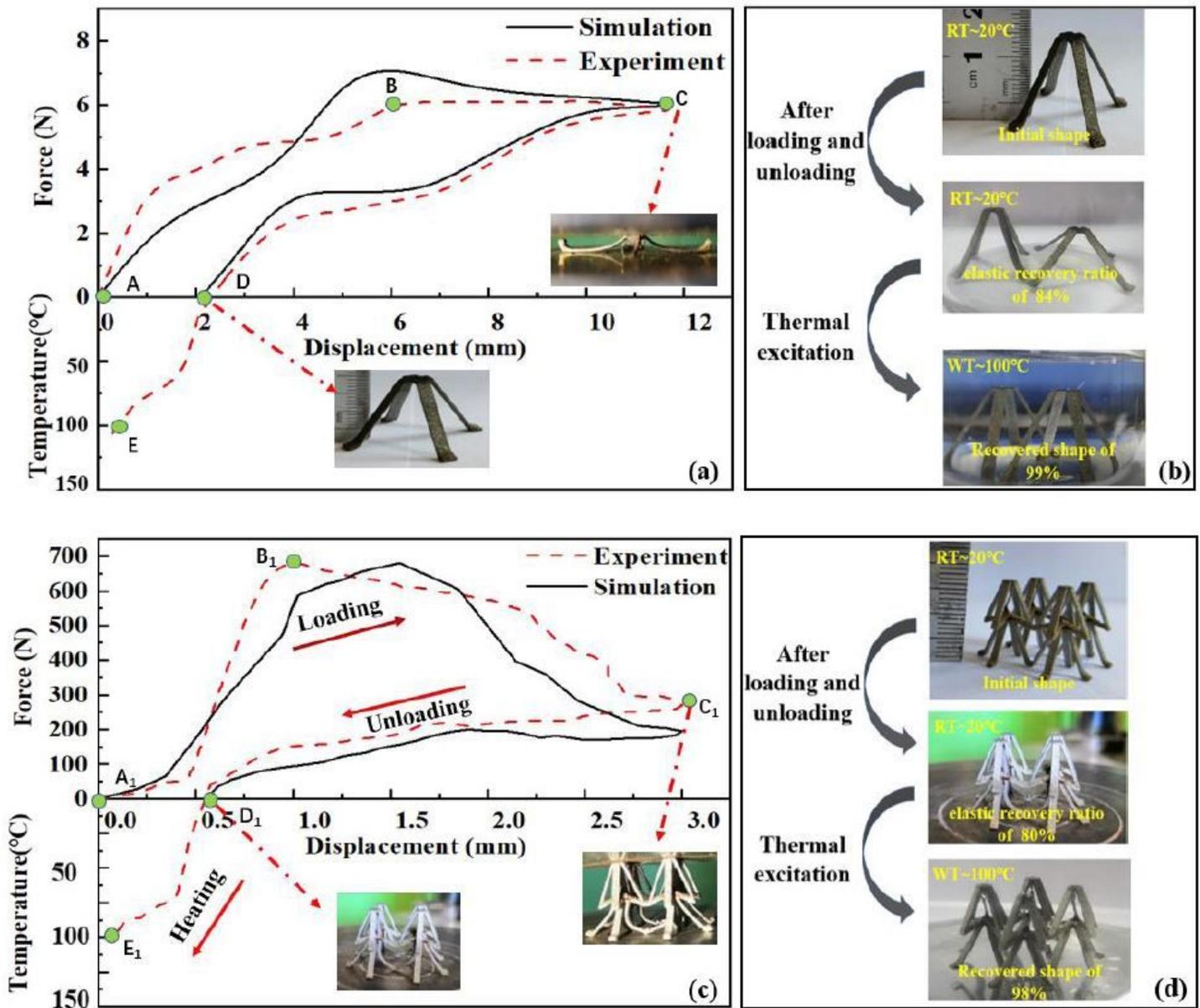
Figure 6

(a) FDT curves acquired through a loading-unloading-heating process of the CS. (b) The shape recovery process of the CS after being heated in a water bath after deformation. (c) FDT curves obtained by loading-unloading-heating processes of the DLS. (d) The shape recovery process of the DLS after being heated in a water bath after deformation

Supplementary Files

This is a list of supplementary files associated with this preprint. Click to download.

- Graphicalabstracts.pdf